AIP | Journal of Applied Physics

Luminescence of Cu2ZnSnS4 polycrystals described by the fluctuating potential model

D. P. Halliday, R. Claridge, M. C. J. Goodman, B. G. Mendis, K. Durose, and J. D. Major

Citation: Journal of Applied Physics **113**, 223503 (2013); doi: 10.1063/1.4810846
View online: http://dx.doi.org/10.1063/1.4810846
View Table of Contents: http://scitation.aip.org/content/aip/journal/jap/113/22?ver=pdfcov
Published by the AIP Publishing

Luminescence of Cu_2ZnSnS_4 polycrystals described by the fluctuating potential model

D. P. Halliday,[1] R. Claridge,[1] M. C. J. Goodman,[1] B. G. Mendis,[1] K. Durose,[2] and J. D. Major[2]
[1]*Physics Department, Durham University, South Road, Durham DH1 3LE, United Kingdom*
[2]*Stephenson Institute for Renewable Energy, University of Liverpool, Liverpool L69 7ZF, United Kingdom*

(Received 18 February 2013; accepted 27 May 2013; published online 11 June 2013)

The growth of Cu_2ZnSnS_4 (CZTS) polycrystals from solid state reaction over a range of compositions, including the regions which produce the highest efficiency photovoltaic devices, is reported. X-ray measurements confirm the growth of crystalline CZTS. Temperature and intensity dependent photoluminescence (PL) measurements show an increase in the energy of the main CZTS luminescence peak with both increasing laser power and increasing temperature. Analysis of the PL peak positions and intensity behavior demonstrates that the results are consistent with the model of fluctuating potentials. This confirms that the polycrystals are heavily doped with the presence of a large concentration of intrinsic defects. The behavior of the main luminescence feature is shown to be qualitatively similar over a broad range of compositions although the nature and amount of secondary phases vary significantly. The implications for thin-film photovoltaic devices are discussed. © *2013 AIP Publishing LLC*. [http://dx.doi.org/10.1063/1.4810846]

I. INTRODUCTION

There are a limited number of renewable energy technologies which have the potential to supply the world's increasing demand for energy at the TW scale. Solar photovoltaic energy conversion (PV) is one of these technologies. Thin-film solar PV will make an increasingly important contribution to the next generation of PV devices as they can be manufactured with highly competitive costs. Thin films have significant potential; the highest thin-film PV conversion efficiency of 20.4% has been reported for a $Cu(In,Ga)Se_2$ (CIGS) device.[1] There has already been significant commercial development of the CdTe/CdS thin-film system with First Solar manufacturing modules based on this system at the GW scale.[2] Predictions based on the availability of constituent elements confirm that CdTe and CIGS technologies can contribute to energy supply in the hundreds of GW range.[3,4] To enable greater deployment of terrestrial PV at the TW level will require: (1) continued, and significant, cost reduction of PV modules; and (2) the ability to manufacture PV devices from sustainable materials.[5] These factors and recognition of the importance of environmental factors including cost and availability of metals and toxicity of PV component elements[6,7] have all led to a significant focus on new sustainable materials for PV devices. Cu_2ZnSnS_4 (CZTS) is recognized as a material system which has the potential to make a substantial contribution to PV generation at a cost that will address the issues discussed above.

CZTS is a sustainable material which has received considerable attention in recent years. It belongs to the I_2-II-IV-VI_4 semiconductor system,[5,8–11] and is a member of the adamantine family.[12] CZTS has been identified as having a direct fundamental energy gap, with a high absorption coefficient, which is close to the maximum of the solar spectrum.[13,14] It has an additional benefit of being fabricated with a range of energy bandgaps depending on the composition of the solid solution although it must also be noted that the full compositional range is not accessible. The highest efficiency device reported to date based on this material system is 11.1% using a mixed S/Se composition for the group VI element;[15] this was produced using a solution-based hydrazine process. The highest efficiency achieved by a vapor deposition process is 9.15%.[16] The highest efficiency achieved with only S for group VI is 6.8%.[17]

Despite the range of successful fabrication strategies for making CZTS devices, which includes sputtering, evaporation, electrodeposition, spray pyrolysis, and ink-based approaches,[14] there is a pressing need for more detailed information about the properties of crystalline CZTS. In this work, a comprehensive photoluminescence (PL) spectroscopy study of solid state grown CZTS polycrystals is reported which investigates the impact of temperature and laser excitation power. Some ambiguity exists regarding PL of CZTS as previous luminescence studies of CZTS single crystals have claimed that the observed luminescence is due to impurities giving rise to donor acceptor pair (DAP) emission.[18,19] More recent studies have proposed a model of fluctuating potentials[4,20] initially developed by Levanyuk and Osipov.[21] Hall measurements have shown that the CZTS system has high doping levels, around $2 \times 10^{20}\,cm^{-3}$, with high levels of compensation predominantly from native defects.[20] Under such circumstances, impurity bands will form in the forbidden energy gap and merge with the conduction and valence bands.

Although the phase diagram of CZTS is not known over the full compositional range,[22] it is known that the compositional region forming stoichiometric CZTS is relatively narrow and that any significant shift in composition results in the formation of a proportion of compounds other than CZTS, referred to as secondary phases. It is expected that

even a modest deviation from the stoichiometric condition will result in the formation of a range of secondary phases such as CuS, Cu_2S, SnS, SnS_2, ZnS, and Cu_2SnS_3.[23]

Empirically, it is observed that the highest performing solar cells are in the Cu-poor, Zn-rich region of the composition phase diagram. Typically, [Cu]/[Zn + Sn] = 0.85 and [Zn]/[Sn] = 1.25 give the best performing devices.[24] Under these non-stoichiometric conditions, the presence of secondary phases is likely to be greater. In general, it has been considered that the presence of secondary phases, particularly when their fundamental energy gap is larger than CZTS, will be detrimental to device performance.[14] Recent work[25] has shown that this may not be the case. The presence of secondary phases at grain boundaries in polycrystalline CZTS alters the grain boundary recombination velocity potentially increasing PV conversion efficiency. In contrast, Chen *et al.* predict, on the basis of thermodynamic arguments, that high quality single crystals, with lower concentrations of intrinsic defects, are most likely to be formed in the Cu-rich, Zn-poor region where the dominant defect is the Cu_{Zn} antisite defect.[26] It is postulated that these conditions may not produce the best solar PV devices because of the relatively large acceptor binding energy of the Cu_{Zn} antisite defect. Chen *et al.* also note that, in the narrow chemical potential region where stoichiometric CZTS can be grown, the dominant self-compensated defect pair complex will be the neutral $[Cu_{Zn}^{-} + Zn_{Cu}^{+}]^0$ complex.[26] This is expected to have poorer charge separation characteristics which will be important when considering PV device performance. This leads to a prediction that the best solar devices will be in the non-stoichiometric Cu-poor, Zn-rich region where V_{Cu} and Zn_{Cu} are anticipated to be the dominant defects.[26] This is consistent with the findings of Katagiri *et al.*[24] There are clear parallels with the copper chalcopyrite system $CuInSe_2$ and $Cu(In,Ga)Se_2$ where it is found that the Cu vacancy defect is prevalent in Cu-poor material and has a low energy of formation. This leads to a range of possible stable defects which have low energies of formation.[27]

Structurally, the CZTS system can exist in the kesterite $I\bar{4}$ or stannite $I\bar{4}2m$ phases.[28] CZTS may also exist in the primitive mixed PCMA $P42m$ structure. This is not considered further in this work as calculations indicate that PCMA has a higher energy structure.[29] Calculations show that the most likely structure for the CZTS system is kesterite[29–31] which is *p*-type from the dominant Cu_{Zn} antisite defect.[26] However, the energy difference between the phases is very small with predicted values ranging from 1.3 meV/atom[30] to ~3 meV/atom.[29,31] The difference between kesterite and stannite phases arises from the ordering of the Cu and Zn atoms.[32] As Cu and Zn are isoelectronic in CZTS, it is not possible to use X-ray diffraction to identify the structure.[33] Evidence regarding the crystal structure of the highest efficiency devices is inconclusive. In addition, the current highest efficiency CZTS PV devices are produced under conditions that do not create a thermodynamically stable CZTS crystalline system.[15–17,34] Other work on the CZTS polycrystals used in this study indicates that they may be disordered on the nanometer length scale.[35] This forms part of a growing body of evidence which suggests that CZTS is a highly disordered phase such that the relationship to ordered kesterite or stannite phases becomes ill-defined.

To provide further insights into the optoelectronic properties of polycrystalline CZTS, low-temperature PL spectroscopy is employed as a powerful, non-invasive technique which gives information about optically active recombination centers, non-radiative pathways, near band edge recombination, and the presence of other optically active levels. By using detailed temperature- and intensity-dependent luminescence measurements, the model of fluctuating potentials is confirmed for the observed PL emission in CZTS polycrystals grown by solid state reaction for all compositions studied. Observed variations in the spectroscopic properties are attributed to the changes in CZTS composition and correlated with the location of CZTS polycrystals on the compositional phase diagram.

II. SAMPLE PREPARATION AND MEASUREMENTS

Sample preparation has been presented previously.[35] In summary: CZTS samples were synthesized by solid state reaction of the constituent elements at 800 °C for 24 h. The purity of the starting elements was chosen to be comparable to the purity of material used for solar PV devices.[14] The purity, as certified by the manufacturers, was Cu (99.9%), Zn (97.5%), Sn (99.85%), and S (99.5%). The dominant impurities in the Zn were listed as Fe and Pb, present in roughly equal amounts. Cu, Zn, and Sn were mixed and placed in a single graphite boat, separate to the S powder contained in a second graphite boat. Both boats were sealed in an evacuated quartz ampoule. After heat treatment, the end of the ampoule away from the graphite boats was first water quenched to condense any sulfur vapor which would otherwise form S-rich secondary phases on the sample surface during cooling. Following this, the entire ampoule was water quenched. A total of eight samples were analyzed in this work. Table I gives the nominal composition based on the weight of the starting components measured using a precision of 0.1 mg.

The samples formed a coating on the graphite boat with no visible evidence of large scale segregation of impurities. All were observed to be polycrystalline with typical grain sizes ranging from 10 to 200 μm. Figure 1 shows a back scattered scanning electron micrograph of sample C4 with the CZTS grains distinctly visible and having typical grain sizes of 50 μm. The image also shows small (~5 μm) secondary phase precipitates decorating the CZTS grain boundaries. EDX quantitative analysis confirmed these secondary phases as CuS. Previous growth of CZTS by this method required annealing for a total of 16 days;[36,37] it has been shown that CZTS polycrystals can be successfully grown in 24 h.

X-ray powder diffraction was performed on the samples to confirm the CZTS structure and explore the possible identification of additional phases. Low temperature PL spectroscopy was performed with the samples mounted under vacuum in a closed cycle helium cryostat. The luminescence was excited by the 458 nm line of an Ar+ ion laser and measured with a cooled Si photodiode array detector connected to a grating spectrometer with a 1200 lines per mm grating.

TABLE I. Composition of CZTS Crystals determined from initial weight of elements. Samples are assigned to one of three PL groups (a)-(c) based on the qualitative appearance of the overall PL spectra.

Number	Composition	Description	[Cu]/[Zn] + [Sn]	[S]/[Cu] + [Zn] + [Sn]	PL group
C1	$Cu_2ZnSnS_{4.8}$	S+20%	1.00	1.20	(b)
C2	$Cu_2ZnSnS_{4.4}$	S+10%	1.00	1.10	(b)
C3	Cu_2ZnSnS_4	Stoichiometric	1.00	1.00	(c)
C4	$Cu_{1.5}ZnSnS_4$	Cu-25%	0.75	1.14	(a)
C5	$Cu_2Zn_{1.25}SnS_4$	Zn+25%	0.89	0.94	(a)
C6	$Cu_2Zn_{1.15}SnS_4$	Zn+15%	0.93	0.96	(a)
C7	$Cu_{1.8}Zn_{1.15}Sn_{0.85}S_4$	Cu-10%, Zn+15%, Sn-15%	0.90	1.05	(b)
C8	$Cu_{2.154}Zn_{0.769}SnS_4$	Cu+7.5%, Zn-23%	1.22	1.02	(c)

A quasi-ternary composition diagram covering the compositional region for these samples is presented in Figure 2. The basis for using the ternary representation is that the amount of S incorporated into the crystals is assumed to depend on the amount of metallic elements. The ternary diagram illustrates the composition regions recognized as Cu/Zn/Sn-rich and Cu/Zn/Sn-poor (denoted by Cu+, Cu-, etc.). It also shows the composition region of the highest performing devices reported to date.[24] The full CZTS phase diagram is extremely complex; however, much useful information can be obtained from a consideration of ternary systems derived from CZTS, as depicted in Figure 2. A study of the quasi-ternary Cu_2S-ZnS-SnS_2 system at 400 °C has shown that, apart from the narrow region at the centre of the plot, there are always additional phases present alongside CZTS.[38] For regions which are Cu-poor, the secondary phases are expected to include $Cu_2ZnSn_3S_8$ and ZnS; regions which are Zn-poor may be expected to have CuSnS, $Cu_2ZnSn_3S_8$, and Cu_2S; regions which are Zn-rich may be expected to have ZnS.[39] Looking at the composition of the samples in Table I, as represented on the phase diagram in Figure 2, they may be placed into four broad groups: group (i) C1, C2, and C3—stoichiometric (noting that C1 and C2 have a S excess); group (ii) C4—Cu-poor, Zn-rich, Sn-rich; group (iii) C5, C6, and C7—Cu-poor, Zn-rich, Sn-poor; and group (iv) C8 Cu-rich, Zn-poor.

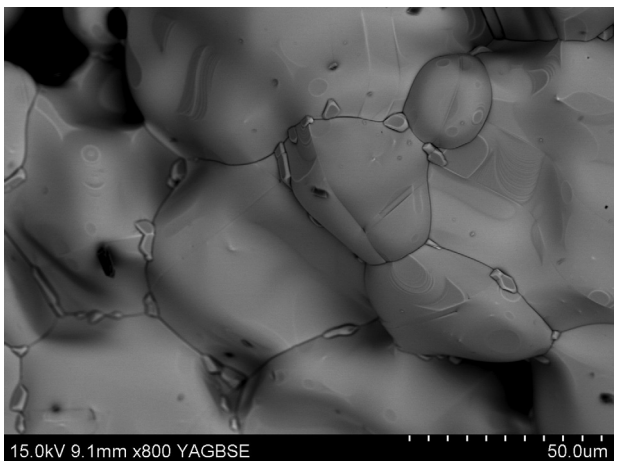

FIG. 1. Back scattered scanning electron micrograph image of sample C4 showing CZTS polycrystals. The small secondary phase crystals decorating the CZTS grain boundaries are identified as CuS from EDX data.

X-ray powder diffraction spectra for all samples are presented in Figure 3. The spectra have been displaced vertically for clarity. The spectra show the reflections expected from the CZTS kesterite phase. The main features present have been identified and are labeled as (101) at 18°, (112) at 28°, (200) at 30°, (220) at 47°, (312) at 56°, (332) at 76°, and (424) at 88° and correspond with the JCPDS CZTS pattern (JCPDS No 26–0575). Less intense features have not been labeled for clarity; however, features present in all spectra correspond with a known peak in the JCPDS pattern. It is recognized that it is not possible to distinguish between the kesterite and stannite phases using X-ray analysis.[33,40] There is also significant overlap in the diffraction pattern of CZTS and common secondary phases, most notably ZnS[40] and Cu_xSnS_{x+1}.[41] The only pronounced variation between the samples in Figure 3 is the additional peak in sample C8 at 27°, highlighted with an arrow, attributed to an unidentified secondary phase. The principal peaks in the X-ray data were used to obtain the average lattice parameters giving $a = 5.425$ Å, $c = 10.86$ Å with $c/a = 2.002$. This compares with previously published values of 5.434 Å and 10.856 Å.[42]

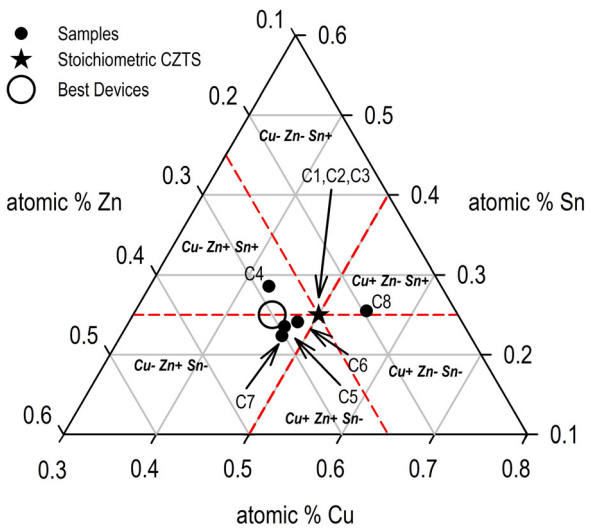

FIG. 2. Quasi-ternary plot based on the atomic percentage of Cu, Sn, and Zn in the samples. The plot also shows the stoichiometric point for Cu_2ZnSnS_4 (star at the centre of the plot). The composition region which has produced the highest efficiency CZTS PV devices is indicated by an open circle. The dashed lines delineate the boundaries between different composition regions.

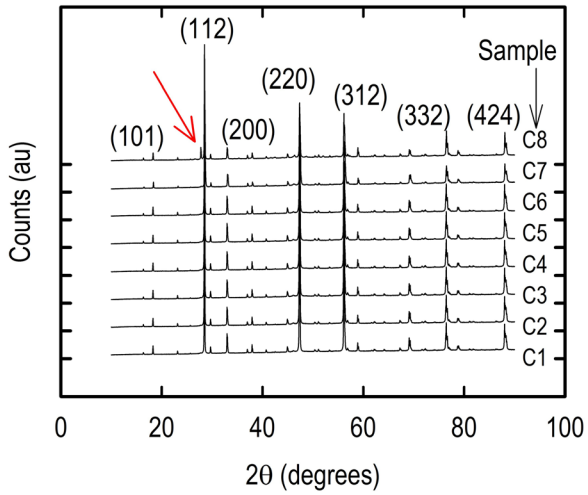

FIG. 3. Powder X-ray diffraction patterns for all CZTS samples. The spectra have been displaced vertically for clarity. The principal features labeled correspond with the JCPDS pattern No. 026-0575 for Cu_2ZnSnS_4. The major identifiable difference in the spectra is an additional peak in sample C8 at 27°, highlighted with an arrow.

These data corroborate the presence of CZTS crystalline material in all eight samples.

Low-temperature PL spectra allowed the samples to be categorized into a smaller set of three broad groups based on the overall qualitative appearance of the spectra. Figure 4 shows PL spectra representative of each of the three PL groups. PL group (a) consists of samples C4, C5, and C6 which have PL spectra characterized by a single dominant feature centered at 1.4 eV which is the main CZTS PL peak. In this group, the main peak has an asymmetry with a tail to higher energy. Samples in this group also show a series of very weak luminescence features in the region 1.6–2.6 eV. PL group (b) consists of samples C1, C2, and C7 which have PL spectra characterized by a dominant CZTS PL feature and in addition a series of relatively less intense features to higher energy in the range 1.6–2.6 eV. In these samples, the main CZTS peak is shifted to lower energies, compared with group (a), and has a smaller FWHM. It also does not exhibit the asymmetry seen in the main CZTS feature from samples in group (a). PL Group (c) consists of samples C3 and C8 which have PL spectra characterized by emission peaks across the full PL range 1.3–2.6 eV having approximately the same intensity; in addition, this group has a CZTS PL feature which is also at a lower energy than group (a) and much weaker in intensity than those in groups (a) and (b). A comparison of Figures 3 and 4 verifies that PL provides a more sensitive measure of the impact of the structural differences and the presence of secondary phases in CZTS compared with X-rays.

III. RESULTS AND DISCUSSION

A comparison of the PL spectra of samples C1, C2, and C3 is shown in Figure 5. These samples all have the CZTS stoichiometric ratio of metallic elements with sample C3 also having the stoichiometric ratio of S. Sample C2 has 10% extra S and sample C1 has 20% extra S. There is no observable difference in the X-ray plots in Figure 3.

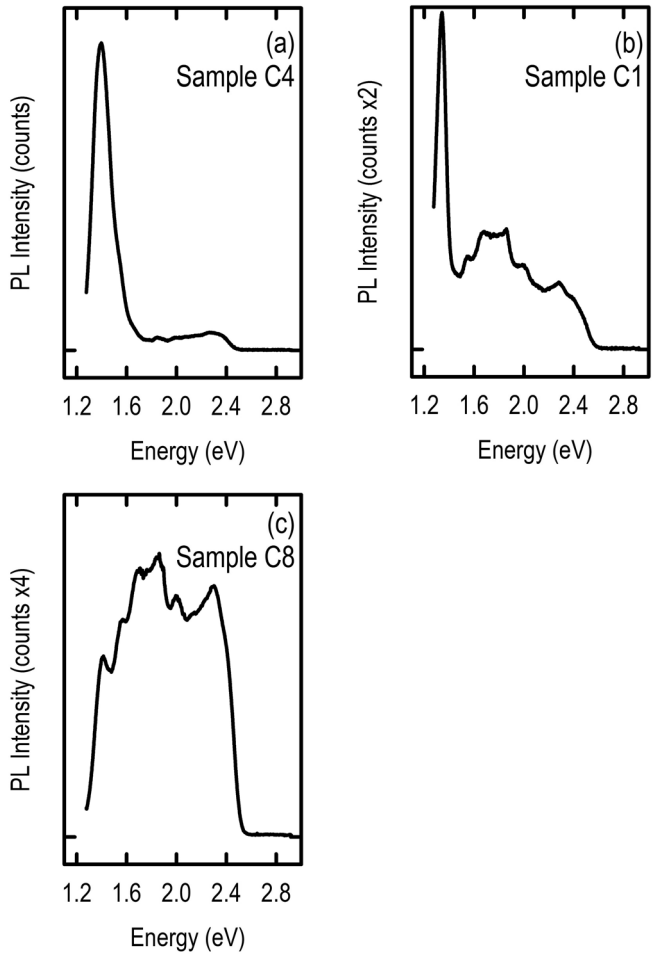

FIG. 4. PL spectra from samples C4, C1, and C8 showing common features of samples in PL groups (a), (b), and (c), classified according to the relative intensity of the main CZTS feature at 1.4 eV. The PL spectra were measured at a sample temperature of 3 K and excited using a laser power of 100 mW at a wavelength of 458 nm.

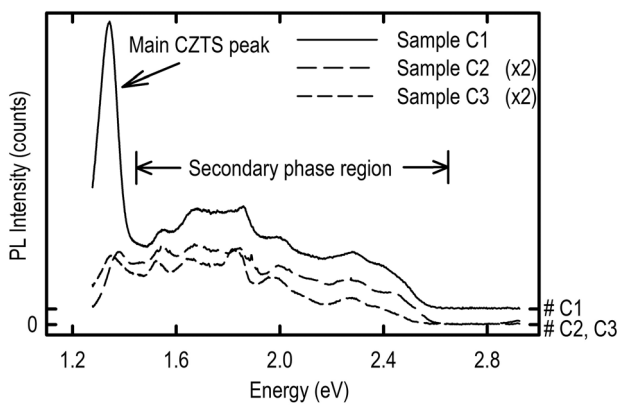

FIG. 5. PL spectra from samples C1, C2, and C3 which all have the stoichiometric ratio of metallic elements. Sample C3 is stoichiometric CZTS, sample C2 had 10% excess S and sample C1 had 20% excess S. All spectra were measured at a sample temperature of 3 K using a laser power of 100 mW at a wavelength of 458 nm. The spectrum for sample C1 has been displaced vertically for clarity; the spectra for samples C2 and C3 have been scaled by a factor of 2.

However, the PL spectra show distinct differences. Sample C1 is in the PL group (b) having a distinct CZTS feature at 1.34 eV. The CZTS PL feature is reduced in intensity in samples C2 and C3 with the peak being at 1.40 eV and 1.37 eV, respectively. There are also a number of luminescence features in the energy range from 1.5 to 2.5 eV. As discussed above, these are attributed to secondary phases. The presence of secondary phases, as indicated by the integrated intensity of luminescence in the 1.5–2.5 eV range, is not correlated with the amount of S during growth. All the samples were cold water quenched at the conclusion of growth so the formation of secondary phases will have most likely occurred at the growth temperature. This has implications for device growth as it is clear that excess S affects the formation of secondary phases even when the metallic elements are in the correct ratio. It should also be noted that the sample with the highest amount of S during growth has the most pronounced CZTS peak. The amount of S incorporated in the CZTS system is expected to be controlled by the amount and valency of metallic elements. This has led to a view that the amount of S incorporated into CZTS depends only on the amount of metallic elements, assuming sufficient S is available.[38] This is the assumption underlying the representation of the samples on the quasi-ternary phase diagram shown in Figure 2. It has been shown that for these CZTS polycrystals this assumption has limited validity.

The remainder of this paper focuses on a detailed analysis of the behavior of the main CZTS luminescence feature in the 1.3–1.4 eV range. Figures 4 and 5 demonstrate that the PL spectra also exhibit a range of emission features in the 1.5–2.6 eV range which are attributed to the presence of secondary phase compounds as discussed above. Analysis of secondary phases and their potential impact on PV devices is reported elsewhere.[25] It should be noted that a full analysis of larger bandgap secondary phases using PL will require a shorter laser wavelength than the 458 nm Ar^+ laser line used in these measurements. The PL intensity of the main CZTS feature is obtained through fitting a series of Gaussian peaks to the full PL spectra. The integrated intensity of the main CZTS PL feature is obtained from the Gaussian area. Samples C4, C5, and C6 in PL group (a) and samples C1, C2, and C7 in PL group (b) all exhibited a distinct CZTS feature which was straightforward to fit. Any intensity overlap with nearby PL emission from secondary phase peaks can be readily removed in this process. Samples C3 and C8 in PL group (c) exhibited a much less intense CZTS PL feature. The method is still applicable in this case although the CZTS intensity will have a greater uncertainty for these samples.

Figure 6 presents the evolution of the PL spectra of three representative samples (C4–PL group (a), C1–PL group (b), and C3–PL group (c)) as a function of increasing laser power from 5 mW to 200 mW at a laser wavelength of 458 nm and a sample temperature of 3 K. In these measurements, an unfocussed laser beam is used: 200 mW is equivalent to an excitation density of 2.8 W cm^{-2}.

The data are interpreted within the framework developed by Schmidt *et al.*[43] This model considers all possible radiative and non-radiative transitions across a direct bandgap semiconductor. Using coupled rate equations, the intensity dependence for each possible pathway can be determined.

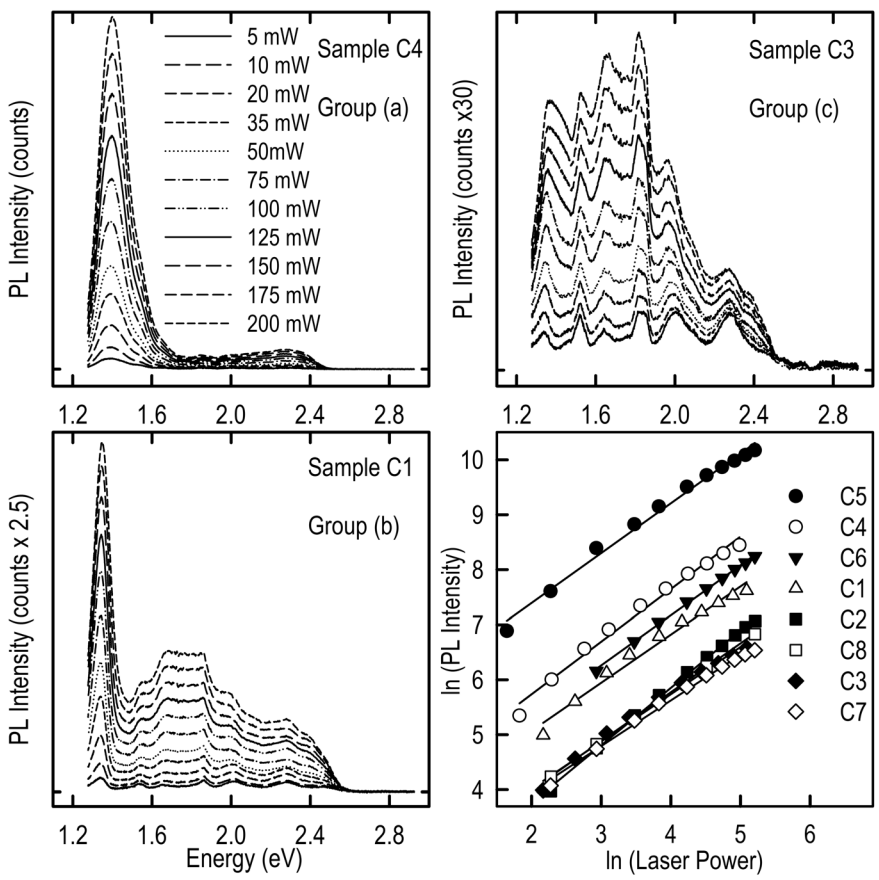

FIG. 6. The evolution of PL emission spectra with increasing laser power for samples C4, C1, and C3 showing behavior typical for sample groups (a), (b) and (c). The ln-ln laser power-luminescence intensity plot shows the behavior of the intensity of the main CZTS PL peak for all samples with increasing laser power. The straight lines are linear regression fits. All measurements were made at a temperature of 3 K.

The model for the dependence of near band edge luminescence intensity with laser intensity explains the $I \propto L^k$ behavior, where I is the luminescence intensity and L is the laser power. The exponent k is shown to be $1 < k < 2$ for excitonic transitions and $k < 1$ for other transitions. The slopes of the linear regression fits to the ln-ln laser power-luminescence intensity plots for all samples in Figure 6 are tabulated in Table II.

With the exception of sample C2, all the slopes are in the range 0.8–1.0. The maximum uncertainty in these data is ±0.05. The k-values are consistent with band-to-band type recombination. Commonly observed k-values for conventional DAP type transitions are 0.2–0.5.[43] It is also observed that, at high laser excitation densities, the PL intensity saturates for DAP type transitions. There is no significant saturation observed in these data. It is likely that the value of 1.05 for sample C2 is a consequence of the relatively low intensity of the CZTS peak as seen in Figure 5. A blue shift is observed with increasing laser power which is one feature of standard DAP luminescence. However, for reasons described below, it can be concluded that the main CZTS peak is not due to conventional DAP recombination from isolated shallow donor and acceptor impurity levels.

It has recently been proposed that the most appropriate model to describe CZTS luminescence is the model of fluctuating potentials.[4,20] This model has also been shown to be appropriate for describing luminescence in Cu(InGa)Se_2.[44]

In heavily doped semiconductors, discrete energy levels associated with shallow impurities, both donor and acceptor, broaden resulting in the formation of impurity bands which ultimately merge with the conduction and valence band density of states into the fundamental energy gap. A large concentration of charged impurities, as is the case in compensated CZTS,[26] gives rise to tail states in the conduction and valence bands. High carrier concentrations produce Coulomb screening of the potential associated with donor or acceptor impurities which reduces their binding energy. The Debye screening radius is given by

$$r_0 = \left(\frac{a_0}{4}\right)^{1/2} \left(\frac{\pi}{3\,n}\right)^{1/6}, \tag{1}$$

where a_0 is the Bohr radius of the isolated shallow donor or acceptor state and n is the concentration of free charge carriers (electrons or holes). The screening radius is significantly less than the Bohr radius of individual impurities. Furthermore, it has been shown that a random distribution of impurities within a volume R^3 has a mean square fluctuation in the number of impurities of $(N_T R^3)^{1/2}$, where N_T is the total concentration of charged impurities, both donor and acceptor. This random distribution of impurities thus has the overall effect of superimposing a fluctuating potential on the conduction and valence band tail states on a length scale of r_0. In a heavily compensated semiconductor, where the mean Fermi level lies in the middle of the forbidden energy gap, the amplitude of the local fluctuating potential is given by

$$\gamma = \sqrt{2\pi}\frac{e^2}{\epsilon\, r_0}\sqrt{N_T r_0^3}, \tag{2}$$

where N_T is the concentration of donor and acceptor impurities and ϵ is the relative permittivity.[45] When the value of γ is more than the binding energy of isolated substitutional shallow donors or acceptors, the fluctuating potential model dominates and the PL spectra behave very differently. In this regime, the energy states contributing to the luminescence are strongly localized.[21] At these high impurity concentrations, it is also necessary to consider the carrier dynamics where changes in the impurity capture cross section can have a profound impact on the luminescence spectrum. At low optical excitation densities and low temperatures, the electrons and holes tend to cluster in lower energy regions of higher donor and acceptor concentration where γ is largest. The maximum separation of donor and acceptor clusters which participate in luminescence transitions under these conditions is determined by carrier tunneling which depends exponentially on their separation.

The temperature dependence of the CZTS luminescence is shown in Figure 7. The thermal activation of luminescence features reveals a considerable wealth of information about the electronic transitions involved in the luminescence process. The temperature dependent intensity of many PL features can be described using a bi-exponential model of the form

$$I(T) = \frac{I_0}{1 + \alpha_1 \exp(-E_1/k_B T) + \alpha_2 \exp(-E_2/k_B T)}, \tag{3}$$

where E_1 and E_2 are independent activation energies for the thermal excitation of charge carriers out of the radiative state to a higher energy non radiative state; this may be an excited state of the optically active centre or a level associated with a completely different centre or defect. The parameters α_1 and α_2 are proportional to the ratio of the degeneracy of the radiative and non-radiative levels.[46] This model describes the temperature behavior of the luminescence transition without requiring a detailed knowledge of the thermal excitation of the optical recombination pathway. There has been some discussion about the validity of such a model to correctly interpret some observed PL emission over a wide temperature range where changes in the capture cross section of one of the levels can provide an alternative explanation.[47] In the case of fluctuating potentials where the thermal excitation of the electron or hole out of the local fluctuating

TABLE II. k coefficients obtained from the slope of the ln-ln laser power-luminescence intensity plots (column 2) (uncertainty in k ± 0.05); fits to Eq. (3) (columns 3 and 4) (uncertainty in E_1 and E_2 ± 5 meV); Increase in CZTS PL peak position from 3 K to 300 K (column 5).

Sample and (PL group)	k	Energy E_1 (meV)	Energy E_2 (meV)	$\Delta E_{300\,K\text{-}3\,K}$ (meV)
C1 (b)	0.85	3	52	66
C2 (b)	1.05	1	32	25
C3 (c)	0.83	3	118	20
C4 (a)	0.96	13	185	23
C5 (a)	0.91	4	42	15
C6 (a)	0.91	11	152	37
C7 (b)	0.83	2	28	72
C8 (c)	0.89	1	51	17

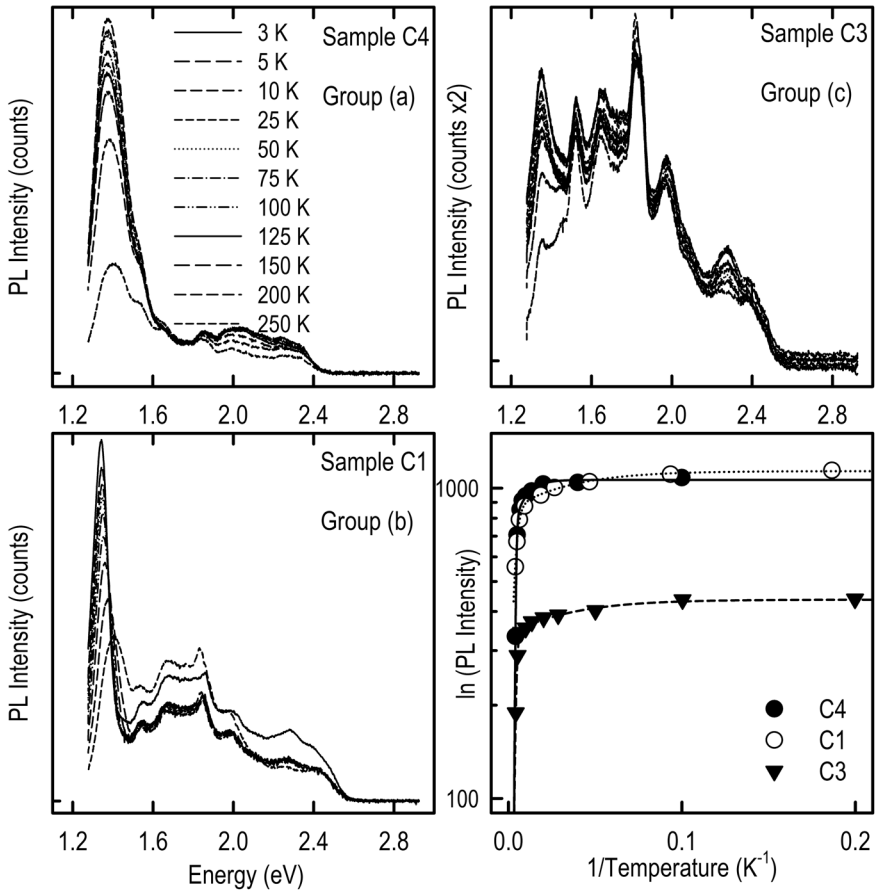

FIG. 7. The evolution of PL emission spectra with increasing temperature for samples C4, C1, and C3 showing behavior typical for sample groups (a), (b) and (c). The Arrhenius plot shows the behavior of the intensity of the main CZTS PL peak for these three samples with decreasing temperature. The lines are fits to Eq. (3). All measurements were made at a laser power of 100 mW.

potential will occur independently with different activation energies, it is appropriate to use the bi-exponential model. Figure 7 shows the PL spectra as a function of temperature for samples C4, C1, and C3 from PL groups (a), (b), and (c), respectively. The bi-exponential fit to intensity of the main CZTS peak for these three samples is also shown in Figure 7 as an Arrhenius plot. Comparable fits are obtained for all samples. The parameters E_1 and E_2 from the fits for all samples are given in Table II.

It can also be seen from the three sets of PL spectra in Figure 7 that the temperature behavior of the secondary phase PL peaks is very different from the main CZTS peak. The intensity of the luminescence in the secondary phase region changes significantly less with increasing temperature. A detailed analysis of this behavior is not discussed for the reasons described above.

The temperature dependence of the peak energy of the main CZTS peak is shown in Figure 8. In all cases, there is an increase in the peak energy from 3 K to 300 K as predicted by the fluctuating potential model. Samples C1, C2, C3, C7, and C8 show a monotonic increase in energy. This corresponds with samples in PL groups (b) and (c). Samples C4, C5, and C6, all in PL group (a), exhibit a decrease in energy at lower temperatures with samples C5 and C6 showing two turning points. This characteristic S-type behavior has also been observed in CIGS.[48]

In conventional low-doped semiconductors, this PL measurement would exhibit behavior consistent with the fundamental energy gap as this is tracked by near band edge transitions. Optical absorption measurements on solution grown CZTS thin films have shown that the fundamental energy bandgap follows the Bose Einstein model.[49] This model predicts that the energy bandgap is described by

$$E_g(T) = E_g(0) - \frac{2a_B}{\exp(\Theta_E/T) - 1}, \tag{4}$$

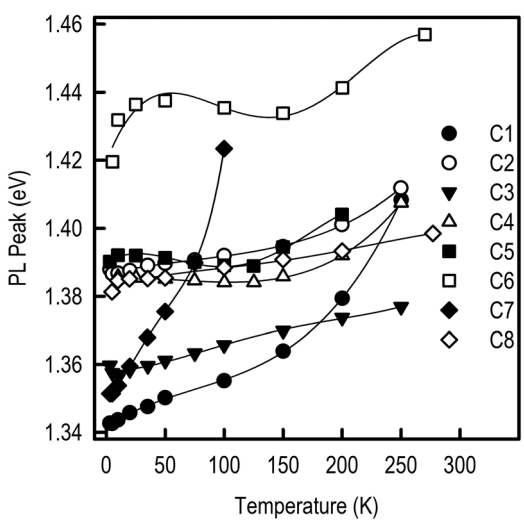

FIG. 8. The temperature dependence of the energy of the main CZTS PL peak for all samples. The lines are a guide to the eye. All measurements were made at a laser power of 100 mW.

where Θ_E is the Einstein temperature and a_B is the electron phonon interaction strength.[50] Although the increase in energy is not linear with temperature, the average value for CZTS has been determined as $\frac{dE_g}{dT} = -8.63 \times 10^{-4}$ eV K^{-1}. This value predicts a decrease of 256 meV in the energy gap of CZTS between 3 K and 300 K. Table II gives the increase in energy in meV observed in the main CZTS peak position between 3 K and 300 K. There is no clear correlation with samples although the two largest shifts are in samples C1 and C7 both in PL group (b).

Figure 9 shows the shift of the main CZTS PL peak with increasing laser power from 5 mW (equivalent to 70 mW cm^{-2}) to 200 mW (equivalent to 2.8 W cm^{-2}). Almost all samples show the same behavior. With the exception of sample C3 (which shows an increase of 45 meV), the average increase is 12 meV. As noted above, the assignment of the main CZTS peak to isolated DAP recombination is not possible. One of the features of normal DAP luminescence is a blue shift as the laser intensity is increased. This would arise from increased Coulomb screening from a larger photoexcited carrier concentration leading to a reduction in the Coulomb interaction in the final ionized state. At higher laser intensities, less distant donor-acceptor pairs would dominate, increasing the energy of the DAP transition. The shift observed here is substantially larger than that normally seen in DAP luminescence (typically a few meV). An estimate of the steady state photocarrier concentration suggests that the highest power used (200 mW) would correspond with the high injection regime. This behavior coupled with the increase in peak energy with increasing temperature suggests that the model of fluctuating potentials is the most appropriate description for this system. The energy shift shows the same behavior for the majority of samples, except C3 and C5, which suggests that similar processes occur in the majority of the CZTS samples despite their very different stoichiometry.

Figure 10 presents a scatter plot of the values E_1 versus E_2 for each sample obtained from the bi-exponential fit. It is

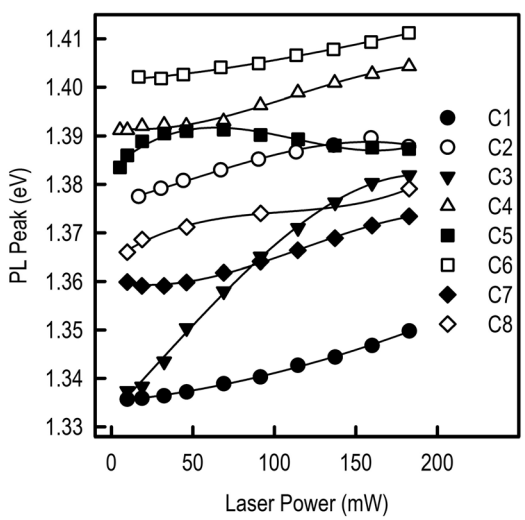

FIG. 9. The laser power dependence of the energy of the main CZTS PL peak for all samples. The lines are a guide to the eye. All measurements were made at a temperature of 3 K.

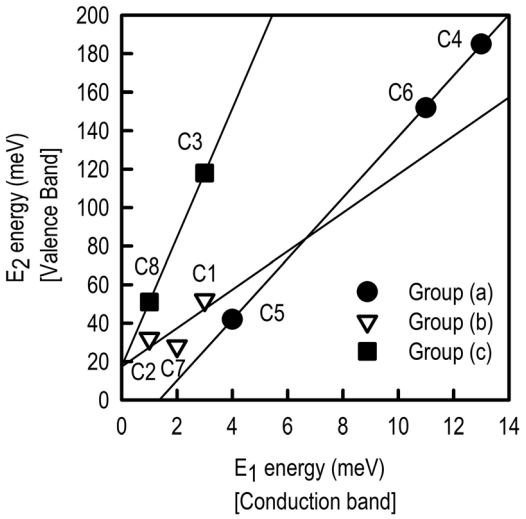

FIG. 10. Values of E_1 and E_2 obtained from the fit to Eq. (3), plotted by PL sample group to show correlation between E_1 and E_2. Lines are linear regression fits to illustrate the degree of correlation between E_1 and E_2.

assumed that the larger E_2 corresponds with the thermal activation of the valence band states. There is evidence of a correlation between the values of E_1 and E_2 for the samples. As the value of E_1 is smaller, it is believed that this represents the thermal excitation of carriers out of local potential wells in the conduction band as the electron effective mass will be less than the valence band effective masses. The value of E_1 is determined by γ, a function of r_0 which in turn depends on the Bohr radius. The values of E_1 also indicate that at all but the lowest temperatures the local potential fluctuations in the conduction band will have negligible effect on the luminescence. It is also worth noting that the three samples which exhibit a more complex temperature behavior in Figure 8 (the three samples in PL group (a)) have the largest values for E_1. It is thus plausible that the interplay between the fluctuations in the conduction and valence bands may explain this behavior. It should be noted that the band gap renormalization introduced by the impurity states will result in the conduction and valence band fluctuations following each other separated by the local renormalized energy gap. According to Shklovskii and Efros,[45] electrons and holes confined by fluctuating potentials can be considered electron and hole droplets with a characteristic dimension (for electrons) of

$$R_e = \frac{a_e}{(Na_e^3)^{1/9}}, \tag{5}$$

where a_e is the electron Bohr radius and N is the density of impurity states. In this model, percolation pathways for electrons and holes out of local potential minima will be different reflecting the different values obtained for E_1 and E_2 in these measurements. The temperature of the intermediate minima in the PL intensity for these three samples, in Figure 8, does correlate broadly with the value of E_1.

It is noted that the FWHM of the PL peaks in group (a) correlates with the larger values of E_1 and E_2 given in Table II and Figure 10. Conversely, the sharper PL peaks

observed for the samples in group (b) correlate with the smaller values of E_1 and E_2. Further work is required to confirm the validity of this observation. The asymmetry to higher energy for the samples in group (a) reflects the reduced probability of carriers occupying higher energy levels within the larger local fluctuating potential. It can be seen from Eqs. (1) and (2) that the size of the local fluctuating potential γ is proportional to $a_0^{3/4}$ where a_0 is the Bohr radius. The Bohr radius, in turn, is proportional to the effective mass of the electron or hole. If it is assumed that the values of E_1 and E_2 are proportional to the size of fluctuations in the conduction and valence bands, we can use the ratio of E_1/E_2 to infer the ratio of the effective masses in the conduction and valence bands. Figure 10 presents E_1 vs. E_2 for each sample. The straight lines are linear regression fits for samples in each PL group (a)–(c). The average slope of the regression fits is 20. If E_1 and E_2 correlated exactly with the values of γ in the conduction and valence bands this would imply that the ratio of the hole to electron effective mass is 54, obtained from $20^{4/3}$. This value is larger than other direct bandgap semiconductors having an energy gap comparable to CZTS. This analysis is not a rigorous method for determining information on the effective mass but nevertheless does suggest that the hole effective mass is larger than the electron effective mass consistent with other direct bandgap semiconductors having a fundamental energy gap similar to CZTS. Very little information exists about the effective masses of carriers in CZTS so further work will be necessary to validate this conclusion. It is clear from a consideration of the fluctuating potential model that this value is likely to be an overestimate of the effective mass ratio as the impact of tunneling has not been included in the model. The thermal activation of electron and holes along differing conduction and valence percolation paths will also limit the validity of this analysis.

The main CZTS peak can also be used to give an indication of the relative size of the energy gap. It is not possible to use PL to determine the energy gap at room temperature in these samples as the PL emission is too weak. However, the relative size of the bandgaps can be readily determined at 3 K. Figure 9 shows the PL peaks for all samples at 3 K. Comparing the positions at the lowest laser power for each sample, it can be seen that the three samples with the largest bandgaps are C6, C4, and C5 which correspond to samples in PL group (a).

It was noted above that the best quality single crystal samples were predicted to be in the Cu-rich, Zn-poor region.[26] This corresponds most closely to sample C8. Figure 4 shows the PL spectra of this sample at 3 K excited using 100 mW of laser power. This sample is in PL group (c). The PL spectrum shows a relatively weak CZTS peak with the spectrum dominated by emission from secondary phases. On the basis of these data, this sample cannot be considered the highest quality.

The relative intensity of the main CZTS peak varies considerably across the samples. This is attributed in part to the relative proportion of secondary phases in the polycrystals and the relatively low carrier lifetime in CZTS as noted above. Notwithstanding this, the general behavior of the CZTS PL peak with increasing temperature and increasing laser power is broadly similar for all the samples across a wide range of compositions. The fact that this behavior is observed over a relatively wide region of the composition phase diagram has implications for PV device application. Although it is known that CZTS has a narrow region of stability in the phase diagram, it has been shown here that the general optoelectronic behavior of CZTS is similar over a much wider composition region where the nature of the secondary phases is likely to vary considerably.

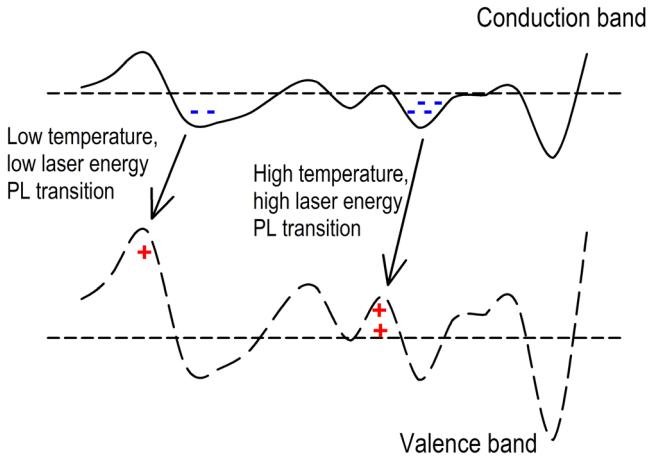

FIG. 11. Schematic showing PL recombination process from fluctuating potentials in the conduction and valence band. The effect of increasing temperature, or increasing laser power, is to increase the PL recombination energy.

Figure 11 shows a schematic of the model of fluctuating potentials in this CZTS material. The fluctuations in the conduction and valence bands will follow each other separated by the local normalized bandgap. Thermal excitation paths out of the local potential wells will be different for electrons and holes as discussed above. At low laser powers and low temperatures, recombination will occur from electrons and holes localized in lower energy potential wells. The maximum separation at which recombination can occur will depend on the tunneling. As the temperature is increased, the effect will be to excite electrons and holes so that they can occupy higher energy states in the potential wells. Thus, PL recombination will be at an increased energy. As laser power is increased, the larger population of photoexcited carriers will occupy higher energy levels within the local potential well also increasing the PL recombination energy as depicted in Figure 11. In this model, local potential wells with larger values of r_0 and γ will demonstrate a larger increase in PL emission energy with increasing laser power and increasing temperature. There will also be a more pronounced asymmetry to higher energy, again consistent with these observations.

IV. CONCLUSIONS

In conclusion, a series of eight Cu_2ZnSnS_4 polycrystals have been grown by solid state reaction at 800 °C for 24 h. The polycrystals had a range of compositions as determined from the starting composition of the elements, including the region known to produce the highest efficiency photovoltaic devices. X-ray measurements confirmed the growth of CZTS crystalline material. All the samples were observed to be

polycrystalline with grain dimensions in the range 10–200 μm. Temperature and laser intensity dependent PL measurements demonstrated that the main CZTS PL peak around 1.4 eV is not due to DAP recombination. The data were fitted to the model of fluctuating potentials which arises from the very high doping level present in CZTS from native defects. The fluctuating potential arises from the mean square fluctuation in the number of impurities in a volume R^3 given by $(N_T R^3)^{1/2}$, where N_T is the total concentration of impurities. The PL data are described by recombination of carriers trapped in local potential wells, previously described as electron and hole droplets. An increase in PL peak position of the main CZTS feature with both increasing temperature and increasing laser power is observed. Fitting data to a bi-exponential function gives independent activation energies for electrons and holes corresponding to different percolation paths for electrons and holes. The data are used to estimate the ratio of the electron to hole effective mass and demonstrate that the hole effective mass is larger. Despite the wide range of compositions, very similar behavior for the main CZTS feature in the samples was observed. The PL data also show evidence of a very broad range of secondary phases. These results make a significant contribution to a body of evidence which points to CZTS being a highly disordered system. In such circumstances, the relationship of CZTS to highly ordered kesterite or stannite phases becomes ambiguous. It has been shown that, despite significant variation in the nature and quantity of secondary phases, the optoelectronic properties of CZTS are dominated by high concentrations of native defects which manifest through the fluctuating potential description of CZTS; the implications for PV devices are discussed.

ACKNOWLEDGMENTS

Financial support for this work is gratefully acknowledged from the Durham Energy Institute (DPH), EPSRC EP/1028781 (BGM) and the RCUK Energy Programme SUPERGEN PV-21 (KD).

[1]EMPA, Science Daily, "Empa takes thin film solar cells to a new level. A new world record for solar cell efficiency," see http://www.sciencedaily.com/releases/2013/01/130118064733.htm (January 18, 2013).
[2]P. Mints, in *The Commercialization of Thin Film Technologies: Past, Present and Future, Honolulu, HI* (IEEE, 2010), pp. 2400–2404.
[3]B. A. Andersson, Prog. Photovoltaics **8**, 61–76 (2000).
[4]M. J. Romero, H. Du, G. Teeter, Y. F. Yan, and M. M. Al-Jassim, Phys. Rev. B **84**, 165324 (2011).
[5]L. M. Peter, Philos. Trans. R. Soc. London, Ser. A **369**, 1840–1856 (2011).
[6]V. Fthenakis, Renewable Sustainable Energy Rev. **13**, 2746–2750 (2009).
[7]V. Fthenakis, MRS Bull. **37**, 425–430 (2012).
[8]T. Todorov, O. Gunawan, S. J. Chey, T. G. de Monsabert, A. Prabhakar, and D. B. Mitzi, Thin Solid Films **519**, 7378–7381 (2011).
[9]H. X. Wang, Int. J. Photoenergy **2011**, 801292.
[10]K. Ramasamy, M. A. Malik, and P. O'Brien, Chem. Commun. **48**, 5703–5714 (2012).
[11]M. Edoff, Ambio **41**(Suppl. 2), 112–118 (2012).
[12]B. Pamplin, Prog. Cryst. Growth Charact. Mater. **3**, 179–192 (1980).
[13]Y. B. K. Kumar, G. S. Babu, P. U. Bhaskar, and V. S. Raja, Sol. Energy Mater. Sol. Cells **93**, 1230–1237 (2009).
[14]D. B. Mitzi, O. Gunawan, T. K. Todorov, K. Wang, and S. Guha, Sol. Energy Mater. Sol. Cells **95**, 1421–1436 (2011).
[15]T. K. Todorov, J. Tang, S. Bag, O. Gunawan, T. Gokmen, Y. Zhu, and D. B. Mitzi, Adv. Energy Mater. **3**, 34–38 (2013).
[16]I. Repins, C. Beall, N. Vora, C. DeHart, D. Kuciauskas, P. Dippo, B. To, J. Mann, W. C. Hsu, A. Goodrich, and R. Noufi, Sol. Energy Mater. Sol. Cells **101**, 154–159 (2012).
[17]K. Wang, O. Gunawan, T. Todorov, B. Shin, S. J. Chey, N. A. Bojarczuk, D. Mitzi, and S. Guha, Appl. Phys. Lett. **97**, 143508 (2010).
[18]K. Hones, E. Zscherpel, J. Scragg, and S. Siebentritt, Physica B **404**, 4949–4952 (2009).
[19]K. Tanaka, Y. Miyamoto, H. Uchiki, K. Nakazawa, and H. Araki, Phys. Status Solidi A **203**, 2891–2896 (2006).
[20]J. P. Leitao, N. M. Santos, P. A. Fernandes, P. M. P. Salome, A. F. da Cunha, J. C. Gonzalez, G. M. Ribeiro, and F. M. Matinaga, Phys. Rev. B **84**, 024120 (2011).
[21]A. P. Levanyuk and V. V. Osipov, Sov. Phys. Semicond. **7**, 721–726 (1973).
[22]G. H. Moh, Chem. Erde–Geochem. **34**, 1–61 (1975).
[23]A. Nagoya, R. Asahi, R. Wahl, and G. Kresse, Phys. Rev. B **81**, 113202 (2010).
[24]H. Katagiri, K. Jimbo, M. Tahara, H. Araki, and K. Oishi, in *The Influence of the Composition Ratio on CZTS-Based Thin Film Solar Cells, San Francisco, CA* (Materials Research Society, 2009), pp. 125–136.
[25]B. G. Mendis, M. C. J. Goodman, J. D. Major, A. A. Taylor, K. Durose, and D. P. Halliday, J. Appl. Phys. **112**, 124508 (2012).
[26]S. Y. Chen, X. G. Gong, A. Walsh, and S. H. Wei, Appl. Phys. Lett. **96**, 021902 (2010).
[27]S. B. Zhang, S. H. Wei, A. Zunger, and H. Katayama-Yoshida, Phys. Rev. B **57**, 9642–9656 (1998).
[28]S. R. Hall, J. T. Szymanski, and J. M. Stewart, Canadian Mineralogist **16**, 131–137 (1978).
[29]S. Y. Chen, X. G. Gong, A. Walsh, and S. H. Wei, Appl. Phys. Lett. **94**, 041903 (2009).
[30]C. Persson, J. Appl. Phys. **107**, 053710 (2010).
[31]S. Y. Chen, X. G. Gong, A. Walsh, and S. H. Wei, Phys. Rev. B **79**, 165211 (2009).
[32]S. Schorr, Thin Solid Films **515**, 5985–5991 (2007).
[33]S. Schorr, Sol. Energy Mater. Sol. Cells **95**, 1482–1488 (2011).
[34]D. A. R. Barkhouse, O. Gunawan, T. Gokmen, T. K. Todorov, and D. B. Mitzi, Prog. Photovoltaics **20**, 6–11 (2012).
[35]B. G. Mendis, M. D. Shannon, M. C. J. Goodman, J. D. Major, R. Claridge, D. P. Halliday, and K. Durose, Prog. Photovoltaics DOI: 10.1002/pip.2279 (published online).
[36]G. P. Bernardini, D. Borrini, A. Caneschi, F. Di Benedetto, D. Gatteschi, S. Ristori, and M. Romanelli, Phys. Chem. Miner. **27**, 453–461 (2000).
[37]S. Schorr, H. J. Hoebler, and M. Tovar, Eur. J. Mineral. **19**, 65–73 (2007).
[38]I. D. Olekseyuk, I. V. Dudchak, and L. V. D. Piskach, J. Alloys Compd. **368**, 135–143 (2004).
[39]J. J. Scragg, *Copper Zinc Tin Sulfide Thin Films for Photovoltaics Synthesis and Characterisation by Electrochemical Methods* (Springer-Verlag, Berlin Heidelberg, 2011).
[40]H. Nozaki, T. Fukano, S. Ohta, Y. Seno, H. Katagiri, and K. Jimbo, J. Alloys Compd. **524**, 22–25 (2012).
[41]P. A. Fernandes, P. M. P. Salome, and A. F. da Cunha, J. Alloys Compd. **509**, 7600–7606 (2011).
[42]P. Bonazzi, L. Bindi, G. P. Bernardini, and S. Menchetti, Canadian Mineral. **41**, 639–647 (2003).
[43]T. Schmidt, K. Lischka, and W. Zulehner, Phys. Rev. B **45**, 8989–8994 (1992).
[44]I. Dirnstorfer, M. Wagner, D. M. Hofmann, M. D. Lampert, F. Karg, and B. K. Meyer, Phys. Status Solidi A **168**, 163–175 (1998).
[45]B. I. Shklovskii and A. L. Efros, *Electronic Properties of Doped Semiconductors* (Springer-Verlag, Berlin Heidelberg, 1984).
[46]D. Bimberg, M. Sondergeld, and E. Grobe, Phys. Rev. B **4**, 3451–3455 (1971).
[47]J. Krustok, H. Collan, and K. Hjelt, J. Appl. Phys. **81**, 1442–1445 (1997).
[48]Y. K. Liao, S. Y. Kuo, W. T. Lin, F. I. Lai, D. H. Hsieh, M. A. Tsai, S. C. Chen, D. W. Chiou, J. C. Chang, K. H. Wu, S. J. Cheng, and H. C. Kuo, Opt. Express **20**, A836–A842 (2012).
[49]P. K. Sarswat and M. L. Free, Physica B **407**, 108–111 (2012).
[50]P. Lautenschlager, M. Garriga, S. Logothetidis, and M. Cardona, Phys. Rev. B **35**, 9174–9189 (1987).